COMMUNICATION

Check for updates

All-day passive radiative cooling using common salts†

Mariana Desireé Reale Batista, [iD] Alyssa L. Troksa, [iD] Hannah V. Eshelman, [iD] Michael Bagge-Hansen [iD] and John D. Roehling [iD]*

Radiative cooling materials underperform compared to their theoretical potential due to parasitic heating from contact with ambient air. Solutions to this problem can be expensive or complex to fabricate. Here, a potentially inexpensive, simply fabricated material that improves cooling performance by reducing parasitic heating was created using naturally abundant salts. NaCl and KCl are not typically considered for radiative cooling because of their high hygroscopicity and low mechanical strength; however, these compounds are highly infrared-transparent and can be fabricated into aerogel-like foam structures to provide thermally insulating properties. The salt foams, described herein, scattered (reflected) visible light, transmitted infrared radiation, and provided thermal insulation. They were packaged into mechanical supporting panels to avoid physical disruption and the nanostructure was stabilized to moisture by adding an anti-caking agent. The panels were able to keep an underlying surface below ambient temperature for a full 24 hour cycle and reduced parasitic heating rate by more than half (compared to an uncovered surface). The panels were able to cool a variety of underlying surfaces, even highly absorbing surfaces that are normally well above ambient temperature during the day. This work demonstrates an affordable, easily produced, electricity-free cooling technology with potential to be manufactured for large-scale practical applications.

New concepts

In this work, we developed a cooling panel that can cool surfaces to sub-ambient temperatures independently or in conjunction with other radiative cooling materials to improve their performance. This panel uses NaCl (table salt) and KCl, which are naturally abundant and highly infrared-transparent materials to insulate a cooling surface while allowing infrared heat to escape. The process is simple, scalable, and suitable for inexpensive mass production. Our implementation also allows the cooling panel to be easily placed and removed without complex installation for seasons when cooling is not desired; other radiative cooling materials are often non-removable. To our knowledge, this is the first example of the use of table salt as a daytime radiative cooling capable material.

1. Introduction

Rising global temperatures are creating an increased demand for cooling; the number of air-conditioning units used worldwide is expected to triple by 2050;[1] however, with 13% of the global population without access to electricity,[2] solutions that can provide cooling without electricity are needed. Passive daytime radiative cooling (PDRC) is a viable method that can provide 24 hour, electricity-free cooling. It is an environmentally-friendly supplement to air-conditioning that can reduce buildings' energy usage, increase power plant efficiency, collect water from the air, and even desalinate water.[3–7]

Thermal infrared (IR) radiation is constantly escaping the earth's surface through the earth's atmospheric transparency window (8 to 13 μm).[8,9] The cold heat-sink of space can therefore be used to absorb heat generated from a surface without additional energy input. This effect can cool surfaces to sub-ambient temperatures.[3] However, when the sun is shining, absorption of solar irradiance (~ 1000 W m^{-2}) typically exceeds the outgoing radiative loss (~ 100 W m^{-2}) making achieving sub-ambient temperature during the day challenging.[10–12] To overcome solar irradiance and achieve all-day radiative cooling, a cooling material must (1) continually lose heat through the atmospheric transparency window and (2) maximize solar reflectance ($> 90\%$, 0.3–2.5 μm) to minimize solar heat gain.[13–15] Materials that can achieve these properties together can successfully achieve PDRC.

Many different approaches have achieved daytime cooling through engineering the optical and IR properties.[16–19] High solar reflectance has been attained using dielectric mirrors backed with reflective metals (such as aluminum and silver),[20,21] photonic crystals,[22] porous paints,[23] or particle films.[22,24]

Materials Science Division, Lawrence Livermore National Laboratory, 7000 East Ave, Livermore, CA, 94550, USA. E-mail: roehling1@llnl.gov

Dielectric mirrors, metals, and photonic crystals work by direct reflection of sunlight, whereas porous and particulate films reflect optical light through Mie scattering, where the particles/pores are approximately the same size as the wavelength they scatter.[13,25] To achieve maximal heat loss through the atmospheric window, high IR emittance is needed. Depending on the application, high IR emission can be either across the whole IR range (*i.e.* blackbody-like, favoring high cooling power) or strongly within the atmospheric window (*i.e.* "ideal" emission, favoring low temperature). Different IR designs have been achieved through engineered emissive layers, such as resonant particles,[24,26] polymers,[27] or metal oxides.[13,28,29]

Most previous work has focused on the emitter to achieve PDRC, but unfortunately parasitic losses from the surrounding air severely limit the ultimate performance of these engineered surfaces. An "ideal" emitter with no parasitic losses should be able to reach up to 60 °C below ambient, but typical performance is limited to several degrees below ambient temperature. This non-ideal performance is because parasitic losses to the air increase as a surface gets colder and providing cooling at low temperatures becomes increasingly difficult. Therefore, methods to insulate the surface, while still allowing radiative cooling to occur, are needed. The ideal material needs to be thermally insulating but maintain high IR transmission in the 8–13 μm band. High IR transmission will not only allow the maximum amount of heat to escape but will also allow increased thickness of the insulating layer, thereby decreasing any parasitic heating. Several groups have focused on these types of insulating materials such as ZnSe windowed vacuum chambers (displaying up to 42 °C below ambient), infrared transparent polyethylene (PE) aerogels, and convection covers.[8,11,30–32] PE aerogels showed promise, demonstrating 13 °C below ambient temperature at solar noon, 18 °C below ambient at night, and the ability to cool a variety of surfaces when placed on top;[11] however, the PE aerogels were complex and potentially costly to fabricate (requiring several solvent exchanges, supercritical CO_2 drying, *etc.*), PE can degrade in sunlight, and PE absorbs IR within the atmospheric window, limiting the maximum usable thickness.

To enable widescale deployment of a PDRC enhancing material, the material needs to be inexpensive and simply fabricated with an easily scaled up process. Previous work has shown that salts can be fabricated into foams using flash freezing and freeze drying.[33] Freeze drying is an industrially used process, easily scaled, and currently used for food and drug production. Here, we developed a simple 24 hour electricity-free cooling material by freeze drying sodium chloride (NaCl) and potassium chloride (KCl) to fabricate optically reflective, IR transparent, and thermally insulating foams. NaCl and KCl are effective alternatives to ZnSe or PE because of their high IR transparency, abundance, and low material cost.

Solutions of NaCl + KCl salts were aerosolized, frozen, and freeze dried under optimized conditions to create highly tunable insulating foam structures. The microstructure and feature size of the salt foams were controlled by changing the salt concentration, salt composition, and solution additives to achieve the properties necessary for radiative cooling. The tunable feature size of the foam provided an opportunity to optimize for high optical reflectivity, while maintaining high IR transmission; the porous structure of the foam provided low thermal conductivity to minimize parasitic heat transfer. These loose foams were packaged into salt foam panels (SFP) with a supporting mechanical frame to minimize mechanical damage. These panels were tested in combination with a broad range of substrate materials. Our results show that these NaCl/KCl foam panels are capable of cooling a variety of sky-facing surfaces below ambient temperatures by up to 10 °C and can improve the performance of well-known radiative cooling materials. These salt foam panels are scalable, easily transferrable from surfaces (important in cold months when passive cooling increases energy use), and economically viable, making them an ideal alternative or addition to other state-of-the-art PDRC devices.

2. Results and discussion

2.1. Salt foam fabrication

The process for preparation of the foam is shown schematically in Fig. 1. An aqueous solution containing NaCl, KCl, sodium
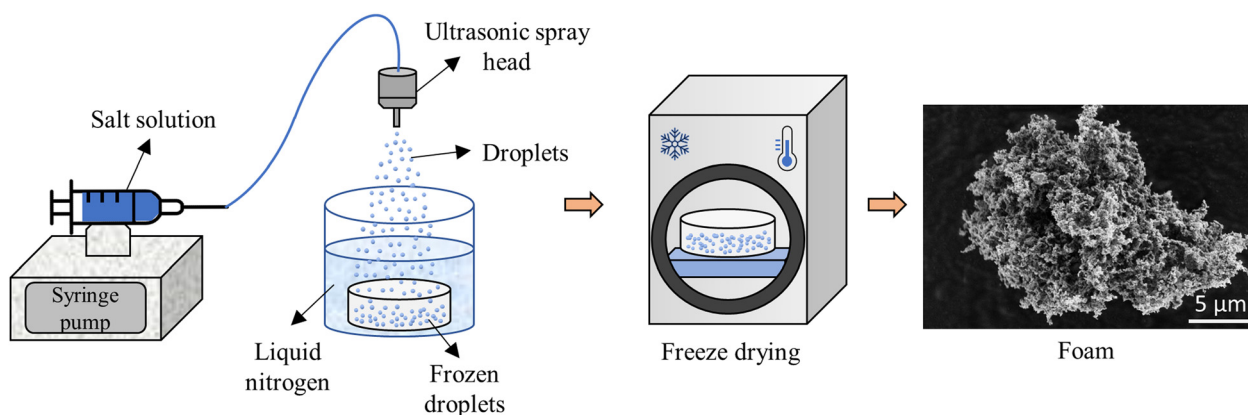

Fig. 1 Schematic illustration of the salt foam fabrication process.

ferrocyanide ($Na_4Fe(CN)_6$) and *tert*-butyl alcohol (TBA) was sprayed directly into a bath of liquid nitrogen to flash-freeze the solution. The frozen droplets were then freeze dried overnight, yielding highly porous foam powder particles with nanoscale features. The rapid solidification using liquid nitrogen was necessary to achieve the desired small feature size. The TBA was added to refine the features of the foams and the $Na_4Fe(CN)_6$ was added to minimize coarsening from moisture. The details of the foam preparation and coarsening mitigation will be discussed in more detail in Sections 2.3 and 2.5. Batches of 5 to 10 g of foam were prepared at once (enough material for one or two cooling panels) and the process took less than one day to prepare. This production method could be easily scaled to kg quantities of foam. In comparison, super-critical CO_2 drying can take up to 3 days for the necessary solvent exchanges and drying processes to complete. Additional technical details on the solution preparation and freeze-drying are given in the Experimental section.

2.2. Outdoor testing

After preparing the foam, it was placed into a mechanical support frame (110 mm [W] × 110 mm [L] × 10 mm [H]) to protect it from mechanical disruption (the foam powders were brittle and were easily crushed by applied pressure) and then encapsulated with thin PE sheets (12.5 μm) to prevent the foam being blown away by wind currents. A diagram of the SFP is shown in Fig. 2a, and an optical image is shown in Fig. S1 in ESI.† The cooling ability of the SFP was demonstrated by

outdoor testing on a hot, clear day. Fig. 2b and c show a schematic illustration and an optical image of the test setup, respectively. Emitters were affixed to polished Cu substrates with thermocouples attached to the bottom of the substrates. Since the cooling performance of an emitter is greatly affected by non-radiative (conductive and convective) heat gains from the surroundings,[12] the bottom of emitters were insulated by polystyrene foam. Several emitting surfaces were tested for comparative thermal performance; (1) white reflective TiO_2 paint, (2) 3M Enhanced Specular Reflector (ESR) film,[20] and (3) black paint, materials which are commonly compared in the PDRC literature.[11,20,25,29] The SFP was placed on top of black paint to serve as a worst-case scenario, where any sunlight transmitted through the SFP would be absorbed and heat the emitter. The testing was performed on 2022 September 8–9 near Livermore, California (peak solar irradiance of 872 W m^{-2}) with the ambient temperature peaking at 42 °C (one of the hottest days of the year). A full 24 hour cycle was measured to demonstrate the uninterrupted cooling capabilities of the SFP. Conditions on the testing day included high wind speeds of up to 10 m s^{-1}, which increases parasitic heating, and high downwelling atmospheric radiation with an average of 381 W m^{-2} (Fig. 3c). The resulting cooling performance of the emitters can be found in Fig. 3a. Note that even the metal-backed 3M ESR film, which has been reported as a sub-ambient cooling film in multiple publications, did not remain sub-ambient in these adverse conditions.[7,11,20]
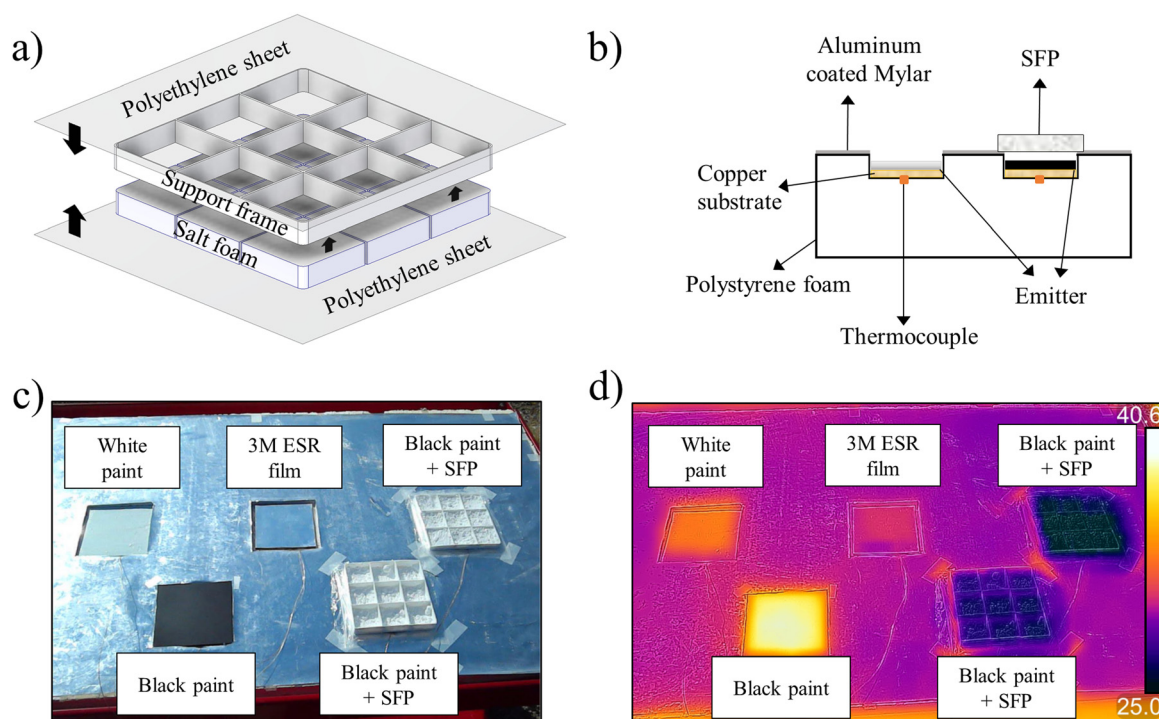

Fig. 2 (a) Illustration of the SFP assembly, (b) illustration of the outdoor testing setup, and (c) an optical and (d) thermal image of the test setup on 2022 September 9 at 9 : 00 AM. Two black painted substrates + SFP with different $Na_4Fe(CN)_6$ concentrations were tested. We reported the results of the black paint + SFP with higher $Na_4Fe(CN)_6$ concentration (1 mM), shown on the top right corner, due to better performance.
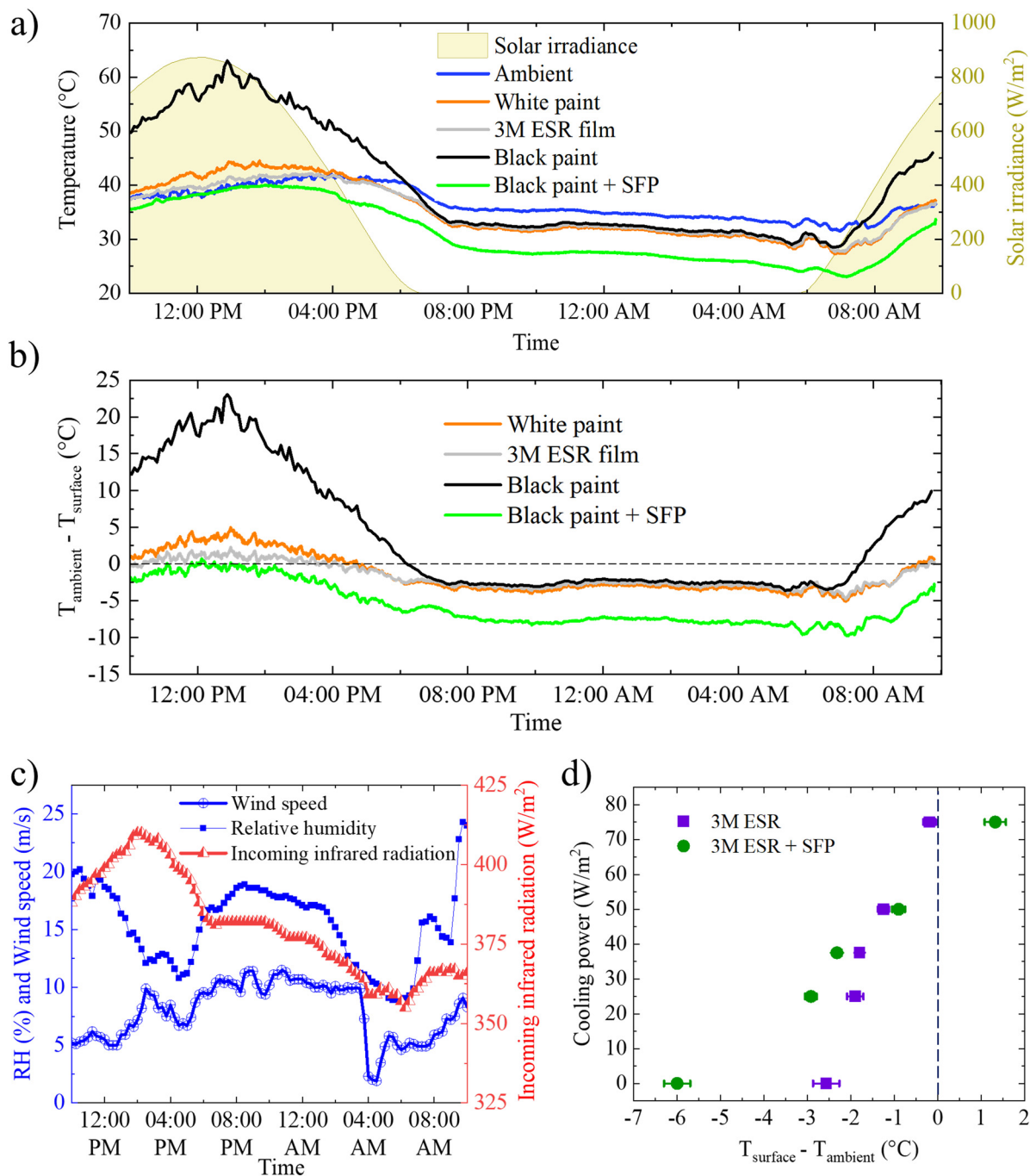
Fig. 3 Outdoor testing data showing (a) measured ambient and emitter surface temperatures (white paint, 3M ESR film, black paint, and black paint + SFP), (b) temperature difference between each surface and ambient, (c) relative humidity, wind speed, and incoming infrared radiation, and (d) cooling power as a function of the temperature drop ($T_{surface} - T_{ambient}$) of an uncovered emitter (3M ESR) and a SFP covered emitter (SFP on 3M ESR).

The SFP kept the underlying black paint below ambient temperature throughout the day, even at solar noon, with a maximum reduction of 10 °C below ambient temperature (Fig. 3b). During the period of highest solar irradiance (from 10 : 30 AM to 04 : 00 PM PST), the SFP covered substrate was the only emitter that remained below ambient temperature. It consistently maintained significantly lower temperatures than the other emitters throughout the day. The SFP reduced the temperature of the black paint (relative to the uncovered paint) by 24 °C during the daytime (12 : 53 PM) and by 5 °C during the night (12 : 00 AM). The SFP also outperformed highly reflective TiO_2 white paint, and the state-of-the-art 3M ESR film[20] which has been commercially used for radiative cooling applications.[6,7,34] Compared to the 3M ESR film, the SFP was 2.1 °C cooler at solar noon and it demonstrated an average temperature drop below ambient of 5.5 °C throughout the day

while the 3M ESR film's average was 1.7 °C. The difference in temperature can be clearly seen in the IR thermal images of the emitters during outdoor test (Fig. 2d).

We attribute the performance advantages of SFP to the reduction of parasitic heating from the environment. Although the presence of the SFP decreases the overall IR transmission from the emitter surface, at low temperatures the insulating properties outweigh transmission losses. Fig. 3d shows the cooling power performance improvement due to using the SFP. Two identical 3M ESR films, affixed to aluminum substrates and backed with resistive heaters were tested. One film was left uncovered and the other was covered with the SFP. These were tested under identical conditions, at the same time and location to ensure performance differences observed could be directly attributed to the presence of the SFP. The SFP begins to outperform an uncovered surface at approximately 1.5 °C below ambient. Below this temperature, the SFP provides higher cooling power than the uncovered surface. The SFP also had a greater maximum temperature drop. The uncovered surface was limited to < 3 °C while the SFP achieved up to 6 °C below ambient, due to the decrease in parasitic heating by the insulating SFP. To quantify the reduction in the parasitic heating rate, the parasitic heat transfer coefficients were measured with and without the SFP, using the method described by Fan *et al.*[35] In this method, the cooling power at ambient

temperature and the maximum temperature drop are measured simultaneously with two identical devices. The uncovered 3M ESR surface was found to have a parasitic heat transfer coefficient of $h = 8.1$ W m^{-2} K^{-1}. Covering the 3M ESR film with the SFP reduced the parasitic heat transfer rate by more than 50%, to $h = 3.6$ W m^{-2} K^{-1}.

2.3. NaCl + KCl foam structure

The structure of the salt foam is responsible for the cooling properties of the SFP. The feature sizes give it its favorable optical and IR properties, while the low density and porosity provide the favorable thermal properties. By controlling the freezing conditions of the salt solution and the salt composition, the structure of the foams was controlled. Scattering calculations (Fig. S2, ESI†) revealed that features smaller than approximately 500 nm were required to achieve the desired IR transmission for effective PDRC (~70% over atmospheric window), ideally under 250 nm. Fig. 4a shows a scanning electron microscope (SEM) image of an optimized NaCl + KCl foam particle. Fig. 4b shows the distribution of feature sizes in this foam, with a bimodal distribution centered around 50 and 300 nm. The optimized NaCl + KCl particle was created by changing the salt concentration within the solution, mixing different salts, and adding TBA.

The total salt concentration affected the overall feature size as well as the foam density. The eutectic composition is known
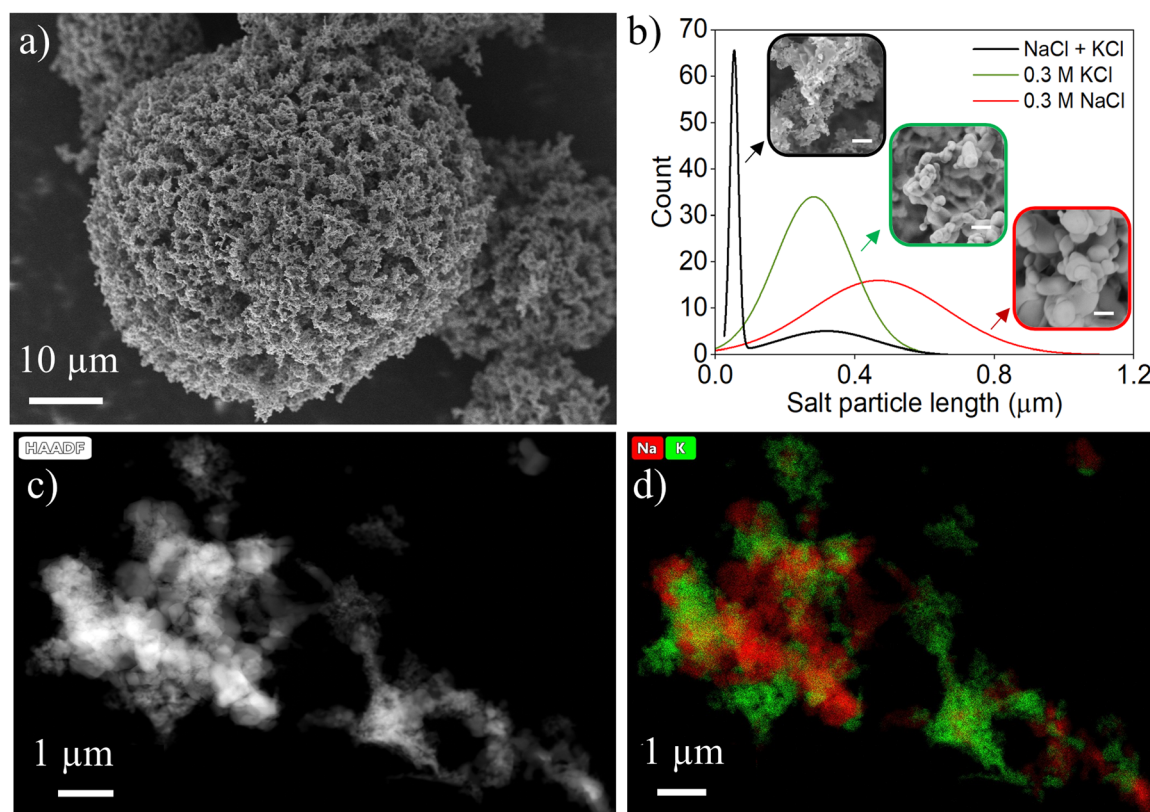

Fig. 4 (a) SEM image of salt foam made from NaCl + KCl with TBA and 1 mM Na$_4$Fe(CN)$_6$, (b) histogram of feature sizes measured *via* SEM from different foams (inset: SEM images of said foams, scale bar 500 nm) (c) TEM high-angle annular dark field image, (d) TEM energy dispersive spectroscopy (EDS) map of a crushed NaCl + KCl particle made with TBA and 1 mM Na$_4$Fe(CN)$_6$.

to result in finer feature sizes due to eutectic-mode solidification.[36] In the NaCl and H_2O solution, hypereutectic concentrations ($>$ 5.1 M) resulted in larger feature sizes than hypoeutectic concentrations ($<$ 5.1 M, Fig. S3 in ESI†). For hypereutectic concentrations, the salt crystals freeze first, and the eutectic structure follows, leaving large proeutectic salt crystals. For hypoeutectic concentrations, H_2O crystals form first, followed by the eutectic structure, leaving only the finely formed eutectic salt crystals. Since the H_2O is removed upon freeze drying, this leaves a highly porous network from the missing large proeuctectic ice crystals making hypoeutectic solutions more favorable for these foams (lower density).

A mixture of salts in solution also resulted in smaller feature sizes since ternary eutectics can form very fine features[36] (NaCl + KCl + H_2O is a ternary eutectic forming mixture). Similar to the case with NaCl + H_2O, the hypoeutectic concentration forced proeutectic H_2O crystals to form first, followed by NaCl + KCl in the eutectic ratio. Fig. 4b shows inset SEM images and feature size distributions of foams made from only hypoeutectic NaCl or hypoeutectic KCl solutions. These foams did not result in sufficiently small features (500 and 300 nm average features, respectively) whereas the mixed salt formed much finer features. The molar ratio of salt to water was around 1%, resulting in approximately 1% dense foam particles as the final density of the loose powder with no packing was approximately 0.02 g cm^{-3}. Transmission electron microscope (TEM) images (Fig. 4c and d) revealed the mixture of NaCl and KCl resulted in small crystallites of each component. Chemical mapping showed larger NaCl features measuring approximately 400 nm and mixture of small KCl features $<$100 nm. This is consistent with proeuctectic H_2O crystals forming first, followed by ternary eutectic formation.

Lastly, the addition of TBA into the salt solution caused further refinement and even distribution of the foam structures (Fig. S3, ESI†). TBA addition has been used to refine micro-structures in freeze cast materials previously.[37,38] The eutectic freezing of ice and TBA causes small domains of TBA and H_2O ice to freeze, distributing small liquid domains of liquid H_2O (with dissolved salt) around the freezing droplet. This is the aforementioned proeutectic freezing of H_2O and drives the concentration of salt up to the eutectic point in the liquid H_2O regions. Subsequently, eutectic freezing of H_2O/salt and any remaining liquid TBA occurs, leaving the fine structures seen in Fig. 4a.

2.4. Optical and thermal properties

A foam with large average feature sizes ($\sim$1 μm) will scatter optical light (*i.e.* sunlight), but will also scatter IR light (due to Mie scattering) leading to low IR transmission.[39] The optimized salt foam with its small feature sizes ($\sim$100 nm) was able to scatter optical light while minimizing IR scattering. The reflectance and transmission of the salt foams were measured by packing the foam into a holder at 2.0% relative density to ensure no gaps. The hemispherical transmittance and reflectance of the foams are shown in Fig. 5a for a 2.5 mm thick layer of powder. The normalized air mass 1.5 (AM 1.5) solar spectrum (U.S. Standard Atmosphere 1976) and the atmospheric transmittance were plotted as a reference.[40,41] The foam had a weighted optical reflectivity of 83% throughout the solar band (weighted by the AM 1.5 spectrum, 0.3 to 2.5 μm) and 86% average transmittance in the atmospheric transparency window (8 to 13 μm). The reported 83% optical reflectance was for a 2.5 mm thick layer, while the SFP used a 10 mm thick layer, which resulted in the higher reflectance required for PDRC of $>$90%. An advantage of using NaCl and KCl is that they have reduced UV absorption relative to other materials such as PE or ZnSe (which absorb UV below 400 nm). Additionally, the IR transmission of the NaCl and KCl do not possess any absorption peaks within the atmospheric transmission window. The peak near 3 μm corresponds to the –OH absorption of water that is present on the surface of the NaCl and KCl. As the
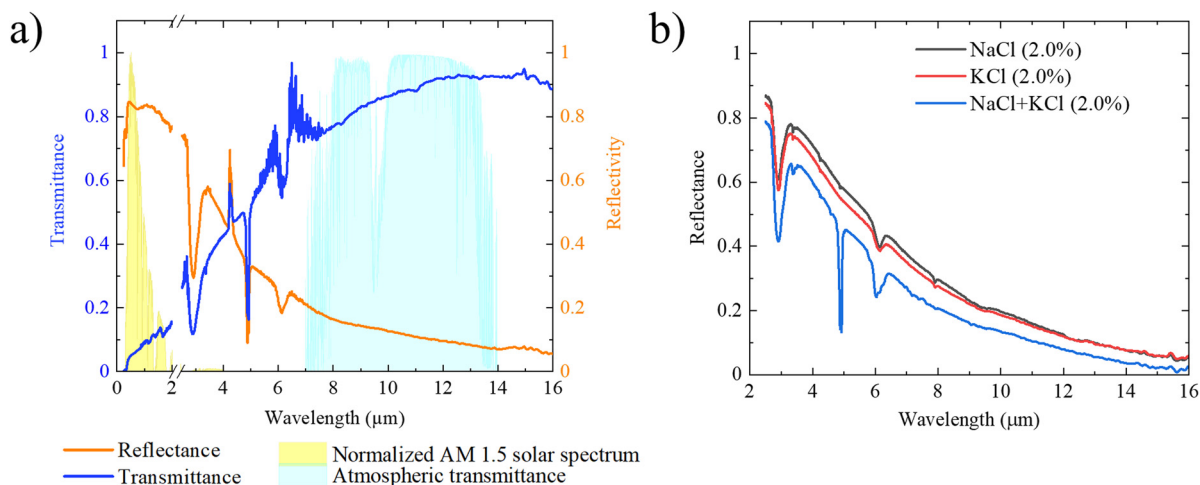

Fig. 5 (a) Hemispherical transmittance and reflectance for a 2.5 mm thick foam layer (2.0% relative density) in the wavelength range of 0.25 μm to 16 μm, along with the normalized AM 1.5 solar spectrum and the atmospheric transmittance. (b) Reflectance of different foams formed from pure salts and the optimized mixed salt foam.

measurements were done in ambient air, moisture was present on the surface of the salt.

The effect of larger features sizes can be seen in the reflectance in Fig. 5b. NaCl foams and KCl foams both had larger feature sizes than the optimized NaCl + KCl foam. The reflectance was the highest for the NaCl (largest features) and lowest for the optimized NaCl + KCl (smallest features). Pure NaCl and KCl foams were found to be ineffective at PDRC because of their lower IR transmission.

If the pores make up a large enough fraction of an foam, the thermal conductivity can reduce by increasing foam density.[42,43] It was unclear if these salt foams were in this regime since they possess a large void fraction. To test how density affected the thermal conductivity, miniature SFPs at two different densities were measured using the hot-disk method. As shown in Table 1, the thermal conductivity exhibited a minimum value of 0.037 W m^{-1} K^{-1} at 1.5% relative density. This conductivity value is similar to other commonly used insulating materials, such as cotton and fiberglass.[44] The measurements suggest that increasing density further will increase the thermal conductivity. Therefore, we packed the SFPs at low density between 1.4–1.5% relative density (0.03 g cm^{-3}), which minimized the thermal conductivity, maximized the IR transmission, and filled any voids after packing the SFP (1% was the lowest self-supporting density possible, but typically resulted in unfilled regions).

2.5. Humidity test

NaCl and KCl are both hygroscopic materials that can easily be recrystallized by ambient humidity resulting in macroscopic shrinkage of the foam and microscopic coarsening of the crystallites. These structural changes reduce the ability of the material to insulate and drastically reduces the IR transmission, rendering the foam ineffective at cooling. Even with encapsulant PE sheets, humidity easily penetrated the SFP and interacted with the salt foams as PE has a high water vapor transmission rate.[43] With recent PDRC works demonstrating continued optimal performance of emitter materials in outdoors environments,[45,46] we sought to improve the longevity of these salt foams. Na$_4$Fe(CN)$_6$ is a well-known anti-caking agent and has been used to stop coarsening of salts from ambient moisture. Previous work has shown that [Fe(CN)$_6$]$^{4-}$ ions replace [NaCl$_5$]$^{4-}$ clusters on the surface of NaCl and must be removed for crystal growth to continue (due to charge mismatch). Since Na$_4$Fe(CN)$_6$ is tightly bound, it creates pinning sites that increase the energy cost of crystallization[47] and is effective at preventing NaCl or KCl crystal growth.

An experiment to demonstrate the ability of the Na$_4$Fe(CN)$_6$ to mitigate coarsening was performed by preparing uncoated and Na$_4$Fe(CN)$_6$ "coated" foam samples. The "coating" was achieved by simply adding the desired Na$_4$Fe(CN)$_6$ concentration to the salt solution before spray freezing. Two miniature SFPs were placed in a humidity chamber for 30 minutes, removed, photographed, then exposed to the next humidity step. For the uncoated SFP, coarsening can easily be seen by macroscale shrinkage of the foam within the frame (Fig. 6, top row). The macroscale shrinkage is indicative of microscale coarsening as seen in the inset images in Fig. 6. Addition of 1 mM Na$_4$Fe(CN)$_6$ reduced the propensity of the coated foams to coarsen from moisture in relative humidities (RH) as high as 75% (Fig. 6, bottom). The Na$_4$Fe(CN)$_6$ coated sample showed only localized coarsening after exposure to 75% RH (bottom inset in Fig. 6). In contrast, the uncoated samples coarsened extensively after being exposed to 75% RH. There is no noticeable macroscale shrinkage of the coated SFP at 55 or 65% RH. The humidity testing clearly indicates that Na$_4$Fe(CN)$_6$ preserves the foam structure and allows the material to be placed outside in local ambient conditions (RH > 60%) without its structure being changed drastically. Testing the SFP outdoors for multiple days resulted in minimal reduction of performance despite humidities up to 75% (Fig. S4, ESI†).

Na$_4$Fe(CN)$_6$ concentrations in excess of 1 mM were found to be unnecessary and did not result in improved moisture resistance. Increasing the concentration of Na$_4$Fe(CN)$_6$ to 10 mM not only did not improve the moisture resistance, but caused excessive parasitic solar absorption (Fig. S5, ESI†) and SFPs made using this concentration were unable to maintain sub-ambient temperature at solar noon because of the increased parasitic solar absorption (Fig. S4, ESI†).

2.6. Future direction

This technology shows promise for improving the economics of radiative cooling materials as it uses low-cost, abundant materials and scalable production methods while improving the performance of radiative cooling materials. However, there are still optimizations that could improve the material function further. This includes improved freezing methods that can solidify the droplets at faster rates to produce smaller foam feature sizes (feature size decreases with increasing freeze rate). This will increase the IR transmission of the foam and allow thicker devices to be produced, improving insulating power and ultimately making the material capable of achieving lower stagnation temperatures and higher cooling powers. Additionally, improved water vapor transmission barriers available for organic light emitting diodes ($< 1 \times 10^{-6}$ g cm^{-2} day^{-1}, 6 order of magnitude reduction from low density PE)[48] will improve the material longevity, potentially to years of service life, and allow these panels to be used in a wider variety of environments without degrading due to moisture exposure. Lastly, the mechanical frame and encapsulation, necessary for protecting

Table 1 Thermal conductivity of salt foam panels and different insulating materials

Sample	Thermal conductivity [W m^{-1} K^{-1}]
[a]Empty support frame (air)	0.026 ± 0.001
[a]SFP at 1.5% relative density	0.037 ± 0.002
[a]SFP at 2.5% relative density	0.043 ± 0.002
[b]Cotton	(0.035–0.060)
[b]Fiberglass insulation	(0.033–0.040)

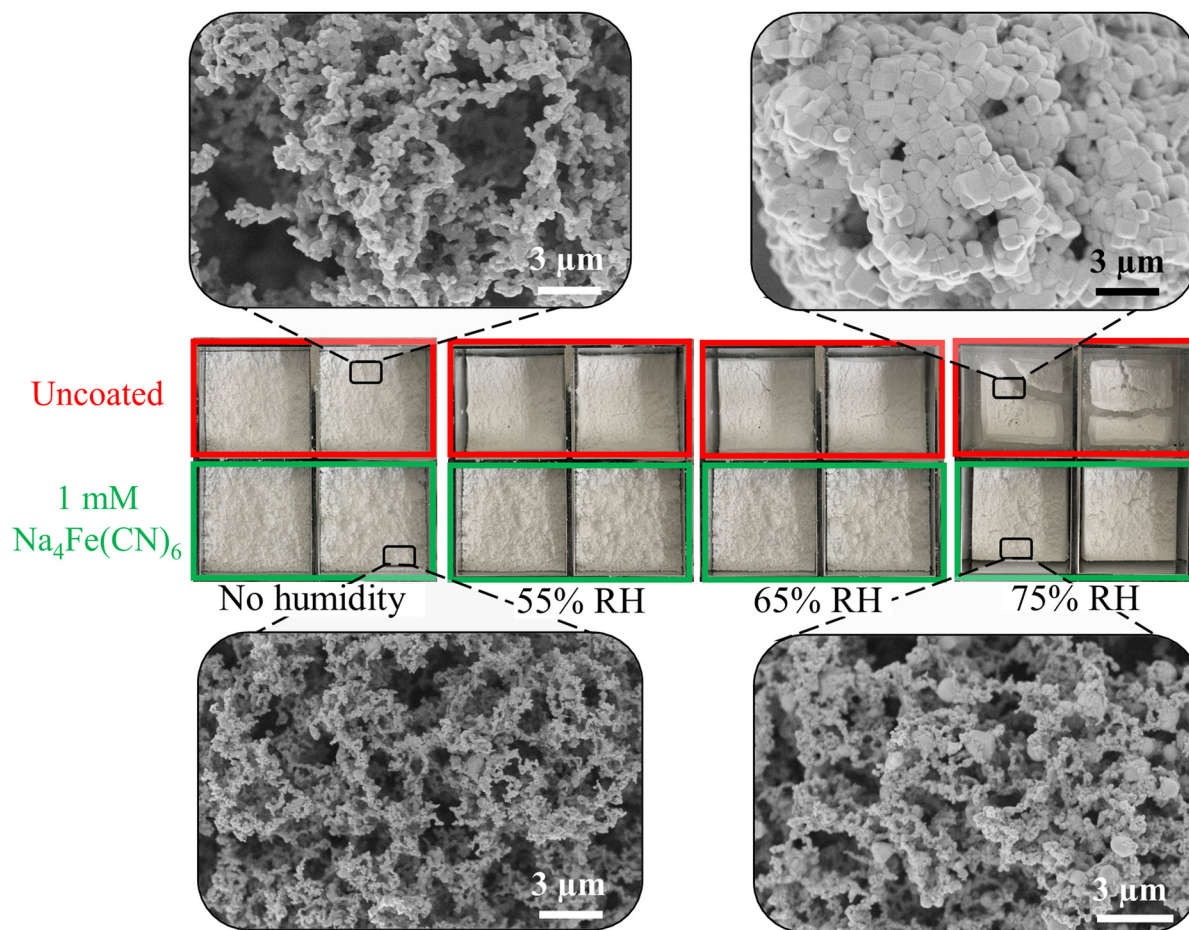[a] Error values shown are the standard deviation in the hot-disk measurement value. [b] Range of values.

Fig. 6 Photos of uncoated foam (top) and 1 mM Na4Fe(CN)6 coated foam (bottom) in different relative humidity conditions, along with SEM micrographs, both before and after moisture exposure.

the fragile loose-packed foam, can be further optimized to maximize the IR transmission and minimize parasitic absorption. This can be done by minimizing the wall area, by encapsulating individual cells of foam rather than the entire device, and having articulating joints in the frame to conform to a wider variety of surface shapes.

3. Conclusions

A simple 24 hour radiative cooling alternative was demonstrated using inexpensive and naturally abundant salts. NaCl + KCl foams with controlled feature sizes were prepared using a simple, scalable, spray-freezing and freeze-drying method, producing foams with high optical reflectivity, high IR transmission, and low thermal conductivity. These foams were packaged into support frames and encapsulated with PE sheets to make foam panels that could cool virtually any underlying surface below ambient temperature. Sub-ambient temperatures were maintained over 24 hours with a maximum temperature reduction of 10 °C. The SFP reduced the parasitic heating rate of a radiative emitter by more than half (h = 8.1 W m^{-2} K^{-1} to h = 3.6 W m^{-2} K^{-1}) by simply being placed on top of the emitter. The SFP consistently

out-performed the commercially available 3M ESR cooling film, averaging nearly 3 °C below the 3M film for the entire 24 hours and 2.1 °C cooler than the 3M ESR film at solar noon on one of the hottest days of the year. This material will enable improved radiative cooling performance for engineered cooling materials, as well as for everyday materials, such as roofs. Given the simplicity of its manufacture and low cost, this technology improves the benefits of radiative cooling since it improves both the lowest achievable temperature and the cooling power at sub-ambient temperature. Possible uses include heat rejection for air-conditioning and power production, direct cooling of buildings, refrigeration, and atmospheric water collection.

4. Experimental section

4.1. Materials

NaCl (ACS, 99.0%) was purchased from Alfa Aesar, Thermo Fisher Scientific, and KCl (ACS) was supplied by LabChem. TBA was obtained from Millipore-Sigma. Sodium ferrocyanide decahydrate (Na$_4$Fe(CN)$_6$·10H$_2$O) was also supplied by Millipore-Sigma.

4.2. Foam synthesis

To prepare the salt foams, an aqueous solution of salt was made with 20.83 g of NaCl to 9.19 g KCl, to 1069.80 g of deionized H_2O (added 1000 g H_2O to ternary eutectic composition). Other additives such as $Na_4Fe(CN)_6$ (1 mM, H_2O basis) or TBA (18 wt% with respect to H_2O) were also added at this point and the solutions were mixed well for several minutes. Next, the solution was pumped through an ultrasonic spray head vibrating at 180 kHz (4.5 W) *via* a Sono-Tek syringe pump to disperse the solution into 5–50 μm droplets. The droplets were sprayed directly into a bath of liquid nitrogen to rapidly freeze. A feed rate of 8 mL min^{-1} was used to minimize build-up of salt on the liquid nitrogen surface. The resulting ice was then kept at -196.2 °C (77 K) until it was transferred into a freeze drier and was lyophilized in a Harvest Right Scientific Freeze dryer with a temperature profile set to -23.2 °C (250 K) for 8 hours, -18.2 °C (255 K) for 6 hours, -9.2 °C (264 K) for 4 hours and -1.2 °C (272 K) for 2 hours and lastly to room temperature until the sample was removed. This profile ensured that the ice was removed while frozen, avoiding any local melting of the salt. Every freeze-dried batch consisted of several containers full of frozen droplets, 25 mL of solution per container was used to ensure that the layer of frozen droplets was thin enough to completely dry in the 20-hour lyophilization cycle.

4.3. Device fabrication

The SFPs fabricated consisted of 3D printed frames of 3×3 squares (each square was 35 mm $\times$ 35 mm $\times$ 10 mm) printed with acrylonitrile butadiene styrene (ABS) and painted with barium sulfate ($BaSO_4$) to minimize solar absorption. The frame was filled with salt foam powder (0.350 g per square, 1.4% relative density) and encapsulated in a thin clear PE sheet (food wrap, 12.5 μm thick) to prevent wind blowing the foam away. The PE sheets were sealed with a heat sealer to make the devices were air-tight. The SFPs were fabricated in a N_2-filled glove box to minimize any initial moisture exposure.

4.4. Outdoor testing

The emitters were mounted in 75 mm polystyrene foam covered with aluminum coated mylar to minimize solar absorption (Fig. 2b). The temperatures of the samples were recorded every 1 minute by type-K thermocouples connected to an Omega RDXL6SD-USB data logger. An onsite weather station was used to determine relative humidity, wind speed and incoming IR radiation. IR thermal radiation images were captured with a FLIR ONE Pro thermal camera.

Parasitic heat transfer coefficients were calculated using a National Instruments 9210 Temperature input module with type-K thermocouples (to monitor temperature) and a USB controlled power supply with a proportional-integral-derivative (PID) controller implemented in LabView to control heater power. 10 cm $\times$ 10 cm silicone encapsulated surface heaters were attached to the bottom of aluminum heat spreader substrates. 3M ESR emitters were affixed to the top of the Al heat spreaders.

The test was conducted at night with minimal wind (< 0.5 m s^{-1}) using identical 3M ESR films and identical SFPs.

4.5. Characterization

The foam microstructure was investigated by SEM in an Apreo S Lo Vac at an accelerating voltage of 2 kV. Fourier Transform Infrared (FTIR) spectroscopy was performed in a Bruker's VERTEX 70 spectrometer equipped with a PIKE Technologies mid-IR integrating sphere. UV-Vis-NIR reflectance/transmittance was measured with a PerkinElmer Lambda 950 with an integrating sphere. Thermal conductivity of an encapsulated support frame without foam, and a SFP packaged with foam at varying relative density was measured in a Hot Disk TPS 3500 Thermal Constants Analyzer (ThermTest Inc). TEM images were collected in a Thermo Fisher Scientific Titan equipped with a SuperX x-ray energy dispersive spectrometer. Particle sizes histograms from SEM images were analyzed by manual measurements in ImageJ.

4.6. Humidity testing

Miniature SFPs (1.5% density) were placed in a Memmert AtmoCONTROL climate chamber. Two SFPs (coated and uncoated foam samples) were held in succession at 55%, 65%, and 75% RH for 30 minutes each and photographed after each exposure. SEM imaging was performed before and after the final moisture exposure.

Author contributions

Mariana Desireé Reale Batista: conceptualization, investigation, visualization, writing – original draft. Alyssa L. Troksa: conceptualization, investigation, writing – review & editing. Hannah V. Eshelman: conceptualization, investigation, writing – review & editing. Michael Bagge-Hansen: conceptualization, writing – review & editing, supervision. John D. Roehling: conceptualization, investigation, writing – original draft, funding acquisition, project administration, supervision.

Conflicts of interest

There are no conflicts to declare.

Acknowledgements

References

1 M.-C. Huang, C.-H. Xue, J. Huang, B.-Y. Liu, X.-J. Guo, Z.-X. Bai, R.-X. Wei, H.-D. Wang, M.-M. Du, S.-T. Jia, Z. Chen and Y. Lai, *Chem. Eng. J.*, 2022, **442**, 136239.

2 Our World in Data, https://ourworldindata.org/energy-access (accessed October 28, 2022).

3 Z. Li, Q. Chen, Y. Song, B. Zhu and J. Zhu, *Adv. Mater. Technol.*, 2020, **5**, 1901007.

4 I. Haechler, H. Park, G. Schnoering, T. Gulich, M. Rohner, A. Tripathy, A. Milionis, T. M. Schutzius and D. Poulikakos, *Sci. Adv.*, 2021, **7**, eabf3978.

5 X. Huang, J. Mandal, J. Xu and A. P. Raman, *Joule*, 2022, **6**(12), 2762–2775.

6 SkyCool Systems, *24/7 Electricity-Free Cooling*, https://www.skycoolsystems.com/, (accessed October 28, 2022).

7 E. A. Goldstein, A. P. Raman and S. Fan, *Nat. Energy*, 2017, **2**, 1–7.

8 Z. Chen, L. Zhu, A. Raman and S. Fan, *Nat. Commun.*, 2016, **7**, 13729.

9 D. Zhao, A. Aili, Y. Zhai, S. Xu, G. Tan, X. Yin and R. Yang, *Appl. Phys. Rev.*, 2019, **6**, 021306.

10 B. Bhatia, A. Leroy, Y. Shen, L. Zhao, M. Gianello, D. Li, T. Gu, J. Hu, M. Soljačić and E. N. Wang, *Nat. Commun.*, 2018, **9**, 5001.

11 A. Leroy, B. Bhatia, C. C. Kelsall, A. Castillejo-Cuberos, M. Di Capua, H. L. Zhao, L. Zhang, A. M. Guzman and E. N. Wang, *Sci. Adv.*, 2019, **5**, eaat9480.

12 M. M. Hossain and M. Gu, *Adv. Sci.*, 2016, **3**, 1500360.

13 J. Mandal, Y. Fu, A. C. Overvig, M. Jia, K. Sun, N. N. Shi, H. Zhou, X. Xiao, N. Yu and Y. Yang, *Science*, 2018, **362**, 315–319.

14 H.-D. Wang, C.-H. Xue, X.-J. Guo, B.-Y. Liu, Z.-Y. Ji, M.-C. Huang and S.-T. Jia, *Appl. Mater. Today*, 2021, **24**, 101100.

15 E. Rephaeli, A. Raman and S. Fan, *Nano Lett.*, 2013, **13**, 1457–1461.

16 B. Zhao, K. Lu, M. Hu, K. Wang, D. Gao, K. Chen, Q. Xuan and G. Pei, *Sol. Energy Mater. Sol. Cells*, 2022, **245**, 111854.

17 X. Yu, F. Yao, W. Huang, D. Xu and C. Chen, *Renewable Energy*, 2022, **194**, 129–136.

18 Z. Ding, L. Pattelli, H. Xu, W. Sun, X. Li, L. Pan, J. Zhao, C. Wang, X. Zhang, Y. Song, J. Qiu, Y. Li and R. Yang, *Small*, 2022, **18**, 2202400.

19 C. Park, C. Park, X. Nie, J. Lee, Y. S. Kim and Y. Yoo, *ACS Sustainable Chem. Eng.*, 2022, **10**, 7091–7099.

20 A. R. Gentle and G. B. Smith, *Adv. Sci.*, 2015, **2**, 1500119.

21 A. P. Raman, M. A. Anoma, L. Zhu, E. Rephaeli and S. Fan, *Nature*, 2014, **515**, 540–544.

22 L. Zhu, A. P. Raman and S. Fan, *Proc. Natl. Acad. Sci. U. S. A.*, 2015, **112**, 12282–12287.

23 J. Liu, Z. Zhou, J. Zhang, W. Feng and J. Zuo, *Mater. Today Phys.*, 2019, **11**, 100161.

24 Y. Zhai, Y. Ma, S. N. David, D. Zhao, R. Lou, G. Tan, R. Yang and X. Yin, *Science*, 2017, **355**, 1062–1066.

25 X. Li, J. Peoples, P. Yao and X. Ruan, *ACS Appl. Mater. Interfaces*, 2021, **13**, 21733–21739.

26 A. R. Gentle and G. B. Smith, *Nano Lett.*, 2010, **10**, 373–379.

27 J. Kou, Z. Jurado, Z. Chen, S. Fan and A. J. Minnich, *ACS Photonics*, 2017, **4**, 626–630.

28 B. Zhao, M. Hu, X. Ao, N. Chen and G. Pei, *Appl. Energy*, 2019, **236**, 489–513.

29 P. Berdahl, *Appl. Opt.*, 1984, **23**, 370–372.

30 A. R. Gentle, K. L. Dybdal and G. B. Smith, *Sol. Energy Mater. Sol. Cells*, 2013, **115**, 79–85.

31 J. Zhang, J. Yuan, J. Liu, Z. Zhou, J. Sui, J. Xing and J. Zuo, *Renewable Sustainable Energy Rev.*, 2021, **143**, 110959.

32 S. N. Bathgate and S. G. Bosi, *Sol. Energy Mater. Sol. Cells*, 2011, **95**, 2778–2785.

33 Lawrence Livermore National Security LLC National Technology, Engineering Solutions of Sandia LLC, *US Pat.*, 11376657-B2, 2018.

34 Passive Radiative Cooling | Energy Conservation | 3M, https://www.3m.com/3M/en_US/energy-conservation-us/applications/passive-radiative-cooling/, (accessed October 28, 2022).

35 F. Fan, D. Xu, Y. Zhu, G. Tan and D. Zhao, *Int. J. Heat Mass Transfer*, 2023, **200**, 123494.

36 S. Akamatsu and M. Plapp, *Curr. Opin. Solid State Mater. Sci.*, 2016, **20**, 46–54.

37 C. Guizard, J. Leloup and S. Deville, *J. Am. Ceram. Soc.*, 2014, **97**, 2020–2023.

38 F. Qian, A. Troksa, T. M. Fears, M. H. Nielsen, A. J. Nelson, T. F. Baumann, S. O. Kucheyev, T. Y.-J. Han and M. Bagge-Hansen, *Nano Lett.*, 2020, **20**, 131–135.

39 H. Kim and A. Lenert, *J. Opt.*, 2018, **20**, 084002.

40 Reference Air Mass 1.5 Spectra, https://www.nrel.gov/grid/solar-resource/spectra-am1.5.html, (accessed October 25, 2022).

41 Atmospheric Transmission Data | Gemini Observatory, https://webarchive.gemini.edu/20210519-sciops--instruments--mid-ir-resources--spectroscopic-calibrations/atmospheric-transmission-data.html, (accessed October 25, 2022).

42 X. Lu, R. Caps, J. Fricke, C. T. Alviso and R. W. Pekala, *J. Non-Cryst. Solids*, 1995, **188**, 226–234.

43 G. Wei, Y. Liu, X. Zhang, F. Yu and X. Du, *Int. J. Heat Mass Transfer*, 2011, **54**, 2355–2366.

44 L. D. Hung Anh and Z. Pásztory, *J. Build. Eng.*, 2021, **44**, 102604.

45 J. Song, W. Zhang, Z. Sun, M. Pan, F. Tian, X. Li, M. Ye and X. Deng, *Nat. Commun.*, 2022, **13**, 4805.

46 C. Cui, J. Lu, S. Zhang, J. Su and J. Han, *Sol. Energy Mater. Sol. Cells*, 2022, **247**, 111954.

47 A. A. C. Bode, V. Vonk, F. J. van den Bruele, D. J. Kok, A. M. Kerkenaar, M. F. Mantilla, S. Jiang, J. A. M. Meijer, W. J. P. van Enckevort and E. Vlieg, *Cryst. Growth Des.*, 2012, **12**, 1919–1924.

48 K.-W. Lu, H.-L. Chen, H.-P. Chen and C.-C. Kuo, *Thin Solid Films*, 2023, **767**, 139672.